Iranian Journal of Basic Medical Sciences
ijbms.mums.ac.ir

Structure-based design of novel and biparatopic anti-PD-L1 nanobodies via CDR grafting and molecular dynamics simulations for enhanced cancer immunotherapy

Mohammad Mehdi Heidari [1]*, Elaheh Jafari Nejad Bidgoli [1], Zahra Mirshamsi [1], Mehri Khatami [1]*, Nima Amadi Afshar [1], Mobina Zare [1]

[1] Department of Biology, Yazd University, Yazd, Iran

ARTICLE INFO

Article type:
Original

Article history:
Received: Jun 6, 2026
Accepted: Sep 23, 2026

Keywords:
Biparatopic nanobody
CDR grafting
Immune checkpoint - blockade
Molecular dynamics - simulations
Single-domain antibody
Therapeutic antibody design

ABSTRACT

Objective(s): In recent years, nanobodies (VHH) have become attractive tools for cancer immunotherapy due to their small size, low immunogenicity, and excellent tissue penetration. Historically, researchers have derived nanobodies from camelid immune libraries, a process that requires animal immunization and complex screening. PD-L1 is a critical immune checkpoint molecule that suppresses T-cell activity by interacting with PD-1. Blocking the PD-1/PD-L1 interaction can reactivate the immune system against tumors.

Materials and Methods: In this study, the complementarity determining region (CDR) grafting approach was applied to engineer a humanized VHH framework by transferring the VH CDRs from the therapeutic antibodies Atezolizumab, Avelumab, and Durvalumab. Based on this strategy, two novel constructs, designated PDL-VHH1 and PDL-VHH2, were generated.

Results: To produce this recombinant protein, the engineered biparatopic nanobody sequence was synthesized and subsequently cloned into the pET-21b(+) vector in an *Escherichia coli* origami expression system. SDS-PAGE analysis confirmed successful production of the biparatopic nanobody. Indirect ELISA showed that PDL-VHH1 had the highest specific binding signal (OD450=1.82±0.14 at 0.130 µM, compared with 1.21±0.09 for PDL-VHH2 and 0.15±0.03 for the control), and both constructs showed concentration-dependent binding to immobilized PD-L1 across 0.0048–0.1305 µM.

Conclusion: These results underscore PDL-VHH1 as a more promising candidate for future therapeutic and diagnostic applications, while PDL-VHH2 serves as a useful binder with moderate affinity. This study establishes a valuable framework for rapidly, cost-effectively, and efficiently designing *in vitro* nanobodies that target immune checkpoints.

▶ Please cite this article as:
Heidari MM, Jafari Nejad Bidgoli E, Mirshamsi Z, Khatami M, Amadi Afshar N, Zare M. Structure-based design of novel and biparatopic anti-PD-L1 nanobodies via CDR grafting and molecular dynamics simulations for enhanced cancer immunotherapy. Iran J Basic Med Sci 2027; 30:

Corrected Proof

Introduction

Cancer is defined by uncontrolled cell proliferation driven by disruptions in the regulatory mechanisms that govern cell division and growth (1). Normal cells and the immune system express a set of immune checkpoints (ICs) that are essential for modulating immune responses. These pathways are critical for maintaining tolerance, preventing autoimmunity, and limiting tissue damage during inflammation. ICs are immunomodulatory proteins, such as PD-1, PD-L1, and CTLA-4, that negatively regulate immune responses (2). PD-L1 (programmed death-ligand 1) is a transmembrane glycoprotein belonging to the B7 family. It is expressed on activated macrophages, certain T and B cells, as well as dendritic and epithelial cells, particularly during inflammatory responses. Importantly, tumor cells exploit PD-L1 expression to evade immune surveillance. PD-L1 is linked to an immune environment characterized by abundant CD8+ T cells and the secretion of Th1 cytokines and interferons. PD-L1 is recognized as a protumorigenic element in cancer cells, functioning by binding to its receptors and activating pathways that promote proliferation and survival. Additionally, PD-L1 facilitates the epithelial-to-mesenchymal transition and induces a stem cell-like phenotype in renal cancer cells (3). The PD-1/PD-L1 axis is a critical pathway in tumor immune evasion. Engagement of PD-L1 on tumor cells with PD-1 on T cells triggers inhibitory signaling through the CD28 pathway. This signaling cascade suppresses T-cell proliferation and activation, reduces cytokine production, and impairs cytotoxic T-cell function. Ultimately, this leads to T-cell exhaustion and apoptosis, thereby dampening the antitumor immune response (4). The primary issue with existing cancer therapies, such as chemotherapy, is their inability to differentiate between normal cells and cancerous

***Corresponding authors:** Mohammad Mehdi Heidari. Department of Biology, Yazd University, Yazd, Iran. Tel: +98-353-1233381, Fax: +98-353-8210644, Email: heidarimm@yazd.ac.ir; Mehri Khatami. Department of Biology, Yazd University, Yazd, Iran. Tel: +98-353-1233013, Fax: +98-353-8210644, Email: m.khatami@yazd.ac.ir

© 2027. This work is openly licensed via CC BY 4.0.
This is an Open Access article distributed under the terms of the Creative Commons Attribution License (https://creativecommons.org/licenses), which permits unrestricted use, distribution, and reproduction in any medium, provided the original work is properly cited.

cells. Furthermore, these treatments can result in a variety of severe and permanent side effects, as well as the development of drug resistance (5). Conversely, innovative therapies that harness the immune system can more precisely target tumor cells, enabling the development of novel anticancer medications. By engineering and producing antibodies directed against a specific antigen on tumor-cell surfaces, treatment can be made more precise (6).

Immune checkpoint inhibitors (ICIs) represent a class of cancer immunotherapies that bolster antitumor immune responses. In certain situations, these medications can provide long-lasting effects with reduced toxicity. Unlike conventional therapies, ICIs rejuvenate and activate the host immune system to combat tumor cells (7). Antibodies targeting immune inhibitory receptors, including CTLA-4, PD-1, and PD-L1, have been widely used as immunotherapeutic agents over the past decade (8). The U.S. Food and Drug Administration has approved three PD-L1 inhibitors, Atezolizumab, Durvalumab, and Avelumab, for application in specific solid tumors (9). Monoclonal antibodies are antibodies generated against a particular antigen. These antibodies are used for various applications, including immunotherapy, because of their exceptional specificity and affinity. Nonetheless, a notable drawback of monoclonal antibodies is their complex structure; their elevated molecular weight and disulfide bonds require production in mammalian cells, which increases costs (10).

Nanobodies are a specific type of antibody found predominantly in the peripheral blood of camelids, including llamas, camels, and alpacas, and they address key challenges and limitations of traditional antibodies (11). Compared with monoclonal antibodies, nanobodies have a lower molecular weight and lower immunogenicity, along with enhanced stability and tissue penetration. They bind their respective antigens swiftly and with high specificity, while the kidneys filter out unbound nanobodies because their small size (~15 kDa) falls below the glomerular filtration threshold. Lacking a light chain and CH1 domain, the antigen-binding region consists solely of the heavy-chain variable region, which is why they are called single-domain antibodies, VHHs, or nanobodies (12).

Antigen-specific nanobodies are typically derived from three genetic sources: immunogenicity, natural libraries, and synthetic libraries. The immunogenicity approach requires animals, while constructing nanobodies from natural and synthetic libraries demands large libraries and complex selection techniques (13). A novel strategy for designing and constructing nanobodies involves isolating the complementarity-determining regions (CDRs) from a specific antibody and integrating them into the nanobody's framework, a technique known as CDR grafting. CDR grafting effectively transfers CDRs with favorable binding characteristics to the nanobody framework, thereby enhancing efficiency (14, 15). A biparatopic nanobody is defined as a construct comprising two different VHH domains that recognize two distinct, non-overlapping epitopes on the same target antigen, connected by a flexible peptide linker. This configuration enables simultaneous engagement of two separate epitopes on PD-L1, which can enhance binding avidity, improve functional inhibition, and potentially overcome resistance mechanisms associated with single-epitope targeting. This design strategy is distinct from bivalent nanobodies, which contain two identical binding domains recognizing the same epitope (16, 17). The design of biparatopic nanobodies capable of simultaneous binding to distinct PD-L1 epitopes could enhance avidity and inhibitory potency. This study addresses this gap by systematically grafting CDRs from three clinically validated antibodies onto the stable Caplacizumab framework, creating a novel biparatopic nanobody with potentially superior binding characteristics and production efficiency. To achieve this, the CDR regions from the antibodies Atezolizumab, Avelumab, and Durvalumab were integrated into the framework of the humanized Caplacizumab nanobody, and the resulting two novel nanobodies were linked together using a linker.

In this study, we designed biparatopic constructs composed of two different VHH domains, both targeting human PD-L1 but recognizing distinct, non-overlapping epitopes on the same antigen. This biparatopic format is distinct from bispecific antibodies, which engage two different target antigens. Following the synthesis of the designed gene and its cloning into an expression vector, the gene sequence was introduced into the *E. coli* origami expression system, and its binding affinity to the antigen was assessed using the ELISA technique.

Materials and Methods

Design of anti-PD-L1 nanobodies

The three-dimensional structures of Atezolizumab, Avelumab, and Durvalumab antibodies, along with the antigen-antibody complex, were retrieved from the Protein Data Bank (PDB codes: 5X8L, 5GRJ, and 5X8M, respectively). CDRs were identified using the IMGT database and grafted onto the humanized framework of the Caplacizumab nanobody (PDB: 5M4W), selected due to its high VH sequence homology (>85%) and proven stability. A flexible $(G_4S)_2$ linker was designed to connect the two nanobody domains. Two novel nanobody constructs were generated: PDL-VHH1, incorporating VH CDRs from Atezolizumab and Avelumab grafted onto the Caplacizumab framework, and PDL-VHH2, comprising VH CDRs from Atezolizumab and Durvalumab within the same Caplacizumab framework.

In the current *in silico* framework, each nanobody (VHH) domain was modeled in complex with PDL1 independently in order to characterize its individual binding mode and interfacial interactions. These models were not intended to imply simultaneous engagement of multiple VHH domains with separate PDL1 molecules. Based on the relative spatial arrangement of the identified binding sites, the two VHH domains recognize adjacent or partially overlapping regions on the PDL1 surface. While this spatial proximity suggests that concurrent binding to a single PDL1 molecule may be feasible with an appropriately designed linker, explicit modeling or dynamic simulation of simultaneous dual engagement was not performed in this study. Therefore, the data support describing the constructs as bivalent, with the potential for biparatopic binding, rather than definitively demonstrating biparatopic engagement at the level of a single PDL1 molecule.

Homology modeling and molecular docking investigations of nanobody structures

The three-dimensional structures of the nanobody constructs were created utilizing the SWISS-MODEL

Corrected Proof

homology modeling server (https://swissmodel.expasy.org/). The amino acid sequences of the VHH domains were submitted in FASTA format, and the server automatically identified appropriate structural templates from the Protein Data Bank (PDB) based on sequence similarity. The highest-scoring templates were chosen according to GMQE (Global Model Quality Estimation) and QMEAN values. The resulting models were visually examined using PyMOL to verify the integrity of the immunoglobulin fold and the orientation of the CDRs.

Molecular docking simulations were conducted utilizing the HADDOCK 2.4 web server (https://haddock.science.uu.nl/). For molecular docking using HADDOCK 2.4, active residues were identified through a multi-step approach. First, the three-dimensional structures of the parental antibody–PD-L1 complexes (PDB: 5X8L, 5GRJ, and 5X8M) were analyzed to identify CDR residues forming direct contacts (distance ≤ 4.0 Å) with the PD-L1 antigen. Second, these residues were cross-validated against published structural and mutagenesis data to confirm their role as binding hotspots in PD-1/PD-L1 interaction studies. Third, interface prediction using the PRODIGY and PISA servers was performed to assess residue contributions to binding energetics independently. Finally, residues were manually inspected using PyMOL to ensure spatial accessibility and proper orientation for antigen recognition. For each VHH domain, the identified CDR residues were designated as 'active' in the HADDOCK docking simulations. In contrast, adjacent framework residues within a 5 Å radius were assigned as 'passive' to facilitate docking. The docking protocol was executed using default parameters, and the resulting complexes were clustered based on interface RMSD.

Molecular dynamics simulation

All molecular dynamics (MD) simulations were conducted to explore the stability and interaction dynamics of the antigen in conjunction with two nanobodies (PDL-VHH1 and PDL-VHH2). We solvated the initial antigen-nanobody complex configurations in a cubic box containing explicit water molecules using the TIP3P water model. The systems were neutralized by adding an appropriate quantity of counterions. Simulations were executed using the Amber99SB-ILDN force field, which is recognized for delivering precise dynamics of proteins and biomolecular interactions. Each system underwent initial energy minimization using the steepest descent algorithm to remove steric clashes. Following this, the systems were equilibrated under an NVT (canonical ensemble) for 100 picoseconds at a constant temperature of 298 Kelvin, regulated by the Berendsen thermostat. This was succeeded by an NPT (isothermal-isobaric ensemble) equilibration for 100ps, employing the Parrinello-Rahman barostat to maintain the pressure at 1 bar. After equilibration, unrestrained production MD simulations were performed for a period of 50 nanoseconds for each complex. All simulations were executed using the GROMACS 2021.4 software package. The LINCS algorithm was employed to restrict bond lengths, facilitating a 2-femtosecond integration time step. Long-range electrostatic interactions were addressed utilizing the Particle Mesh Ewald (PME) method. The resulting trajectories were examined with the integrated tools available in the GROMACS suite. The following properties were computed to evaluate complex stability and interactions: the root mean square deviation (RMSD) of the protein backbone, the root mean square fluctuation (RMSF) of individual residues, the radius of gyration (Rg), and intermolecular hydrogen bonds. Additionally, non-bonded interaction energies (both electrostatic and van der Waals) were calculated between the nanobodies and the individual chains of the antigen. The visualization of the structures and trajectories was conducted using the PyMOL molecular graphics system.

Binding free energy calculations were performed using the MM/PBSA (Molecular Mechanics/Poisson-Boltzmann Surface Area) method implemented in the gmx_MMPBSA tool [1†L4-L7][5†L3-L5]. A total of 200 snapshots were evenly extracted from the last 40 ns of each 50 ns trajectory [6†L27-L29]. The binding free energy (ΔG_{bind}) was calculated as the difference between the free energy of the complex and the sum of the free energies of the isolated receptor and ligand [6†L7-L11]: $\Delta G_{bind} = G_{complex} - (G_{protein} + G_{peptide})$. Solvent and solute dielectric constants were set to 80 and 2, respectively [6†L29-L30]. The polar solvation free energy was calculated by solving the Poisson-Boltzmann equation, while the non-polar contribution was estimated from the solvent-accessible surface area (SASA) [6†L21-L24].

Gene design, synthesis, and cloning

The amino acid sequences of the nanobody constructs were reverse-translated into nucleotide sequences. Codon optimization was performed using the GenSmart™ Codon Optimization tool (GenScript, Piscataway, NJ, USA) to improve expression efficiency in *E. coli*. The optimized sequences were subsequently verified *in silico* to confirm the absence of unwanted restriction sites and ensure manufacturability before commercial synthesis. Pishgaman Gene Transfer Company (Iran) commercially synthesized the designed nanobody genes. After synthesis, the nanobody fragments were cloned into the pET 21b(+) expression vector, regulated by the T7 promoter. The recombinant plasmids were confirmed through restriction digestion and Sanger sequencing to ensure the correct insertion and orientation of the nanobody genes. After sequence confirmation, the recombinant plasmids were supplied lyophilized for subsequent transformation and protein expression studies.

Bacterial host and transformation

The *Escherichia coli* Origami strain (Novagen) was chosen as the bacterial host for the expression of recombinant proteins due to its superior ability to form disulfide bonds within the cytoplasm. Chemically competent cells were generated and transformed with the recombinant pET-21 b (+) plasmids containing the nanobody genes through the heat shock method. After transformation, the cells were spread on LB agar enriched with 50 mg/l ampicillin and incubated at 37 °C for 24 hr. Distinct colonies emerged post-incubation, signifying the successful selection of ampicillin-resistant transformants. To verify the presence of the recombinant plasmids, colony PCR was conducted utilizing gene-specific primers that target the nanobody inserts. The PCR products were examined via agarose gel electrophoresis, and colonies that produced amplicons of the anticipated size were chosen for further expression studies.

Corrected Proof

Expression and purification

The single colonies of *E. coli* Origami containing the verified recombinant pET-21 b (+) plasmids were selected after colony PCR validation. These colonies were then inoculated into LB broth enriched with 50 mg/L ampicillin and cultured overnight at 37 °C while shaking at 200 rpm. The overnight culture was then diluted 1:100 into fresh LB medium with ampicillin and incubated until the optical density at 600 nm (OD600) reached 0.6-0.8. Protein expression was induced by adding isopropyl βD1thiogalactopyranoside (IPTG) to a final concentration of 1 mM, followed by incubation at 37 °C for 4 to 6 hr with shaking. Cells were harvested by centrifugation at 10,000×g for 10 minutes at 4 °C. The cell pellets were then resuspended in lysis buffer and analyzed by SDS-PAGE to confirm recombinant protein expression. Comparisons were made between samples from induced and uninduced cultures to verify the IPTG-dependent expression of the two anti-PD-L1 biparatopic nanobodies. The induced samples showed distinct bands matching the anticipated molecular weights (28.7 and 29.1 kDa), confirming successful expression.

The cell pellet was resuspended in a 1:4 lysis buffer (50 mM Tris-Cl, 1 mM EDTA, pH 8.5) and sonicated for 10 sec in an ice bath with an interval of 20 sec for 20 cycles, then centrifuged at 12,000 rpm for 20 min at 4 °C. After confirming the expression of nanobodies in the form of inclusion bodies, the inclusion bodies obtained from 200 ml of bacterial culture were dissolved in 5 ml of inclusion body solubilization buffer containing 8 M urea and NaH_2PO_4 (100 mM). The resulting pellet was completely solubilized by vortexing, and the solution was incubated overnight at 4 °C. Following incubation, the samples were centrifuged at 20,000 rpm for 20 min to remove insoluble impurities.

The clarified supernatant was then subjected to purification using a nickel affinity column (Ni-NTA). The supernatant was slowly loaded onto the column, after which the column was initially washed with refolding buffer containing 8 M urea. Subsequently, to remove proteins that were nonspecifically bound to the column, washing was performed using refolding buffer containing 17 mM imidazole at 25 °C, and the collected fraction was designated as the second wash. For elution, the column was washed with 5 ml of refolding buffer containing 275 mM imidazole to elute the final nanobody bound to the column via the His tag. After purification, 20 µL of each fraction was loaded onto a 15% SDS-PAGE gel to confirm nanobody presence in the collected fractions. Fractions containing nanobody were transferred into a dialysis bag, and stepwise dialysis was performed to remove urea and prevent improper protein folding gradually. Accordingly, the urea concentration in the surrounding buffer was reduced every 24 hr until it reached zero (6 M, 3 M, 2 M, 1 M, 0.5 M, and 0 M). All dialysis buffers were adjusted to pH 8.0. To facilitate disulfide bond formation and achieve proper folding of the nanobody, oxidized glutathione (GSSG; 375–400 µM) and L-arginine (400 mM) were added to the 1 M urea refolding buffer. The Falcon tube containing the dialysis bag was then incubated overnight at 4 °C. Finally, after complete removal of urea, the dialysis buffer was discarded and replaced with 1× PBS buffer containing NaCl (137 mM), KCl (2.7 mM), NaH_2PO_4 (100 mM), and KH_2PO_4 (2 mM). The sample was incubated for an additional 24 hr at 4 °C. At the end of the refolding process, the refolded nanobody solution was recovered from the dialysis bag, and its concentration was determined using a NanoDrop spectrophotometer (A_{280}). Protein concentration was also confirmed by Bradford assay using BSA as standard. From a 200 ml bacterial culture, approximately 15–18 mg of total inclusion body protein was obtained. After solubilization in 8 M urea and Ni-NTA purification, the clarified supernatant yielded approximately 12–14 mg of solubilized protein. Following stepwise dialysis refolding, approximately 1.5–2.5 mg of purified, soluble nanobody was recovered, representing an overall refolding yield of 10–15% from the initial inclusion body material. The final concentrations of refolded PDL-VHH1 and PDL-VHH2 were 0.85 mg/ml and 0.72 mg/ml, respectively, sufficient for subsequent ELISA characterization. These yields are consistent with previously reported refolding efficiencies for disulfide-bond-rich VHH nanobodies expressed in bacterial inclusion bodies. The final samples were stored at −20 °C for subsequent experiments, including ELISA.

Indirect enzymelinked immunosorbent assay (ELISA)

The binding activity of recombinant nanobodies targeting PDL1 was assessed through indirect ELISA. In summary, 96-well microtiter plates were coated with recombinant PDL1 antigen at a concentration of 5 µg/ml in PBS and incubated overnight at 4 °C. The plates were washed three times with PBST (PBS containing 0.05% Tween-20) and subsequently blocked with 5% (w/v) skimmed milk in PBS for 2 hr at 37 °C to inhibit nonspecific binding. After removing the blocking solution, nanobody samples diluted in PBS were added to the wells and incubated under the same conditions. Following three washes with PBST, the bound nanobodies were identified using an HRP-conjugated anti-6×His antibody (1:1000 dilution) for 1.5 hr at 37 °C. After washing, the TMB substrate was added, and the reaction was allowed to develop at room temperature. The enzymatic reaction was terminated by adding H_2SO_4, and absorbance was recorded at 450 nm using a microplate reader.

Statistical analysis

All statistical analyses were conducted utilizing GraphPad Prism software, version 5.0 (GraphPad Software, San Diego, CA, USA). The data are expressed as mean ± standard deviation (SD) unless specified otherwise. Comparisons between two independent groups were performed using an unpaired Student's *t*test. A *P*value of < 0.05 was considered statistically significant.

Results

Design and construction of biparatopic anti-PD-L1 nanobodies

Using a CDR grafting strategy, two novel biparatopic anti-PD-L1 nanobodies were designed. The three complementarity-determining regions (CDR1, CDR2, and CDR3) from the heavy chain variable domain (VH) of the monoclonal antibodies Atezolizumab (PDB: 5X8L), Avelumab (PDB: 5GRJ), and Durvalumab (PDB: 5X8M) were grafted into the VHH framework of Caplacizumab (PDB: 5M4W). Two distinct biparatopic constructs were generated: PDL-VHH1, comprising VH CDRs from Atezolizumab and Avelumab, and PDL-VHH2, comprising VH CDRs from Atezolizumab and Durvalumab. The two engineered VHH domains in each construct were linked using a flexible $(G_4S)_2$ peptide linker to facilitate tandem antigen engagement. The amino acid sequences and schematic representations of the constructs are provided in Figures 1 and 2.

The 3D models (Figures 1B and 1D) illustrate the interaction between the nanobody constructs and the PDL1 antigen. In the PDLVHH models, the CDR loops point toward the PDL1 binding interface, indicating their direct involvement in antigen recognition. In the biparatopic constructs, both VHH domains are strategically

Corrected Proof

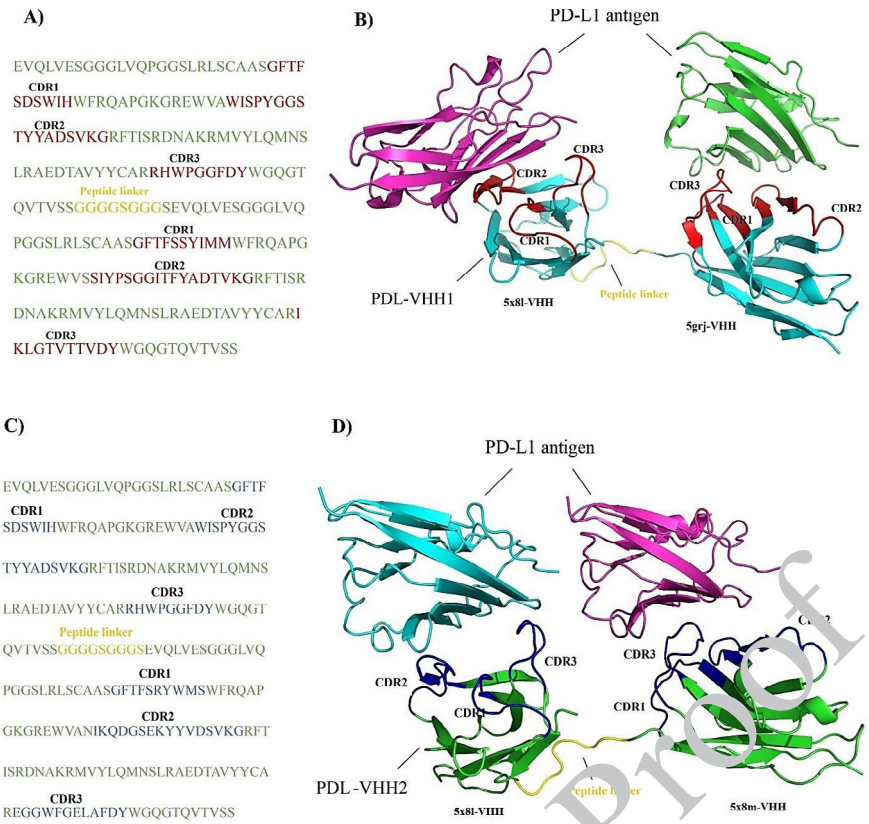


Figure 1. Amino acid sequences of nanobodies PDL VHH1 (A) and PDL VHH2 (C), and schematic representation of their biparatopic structural architectures (B and D)

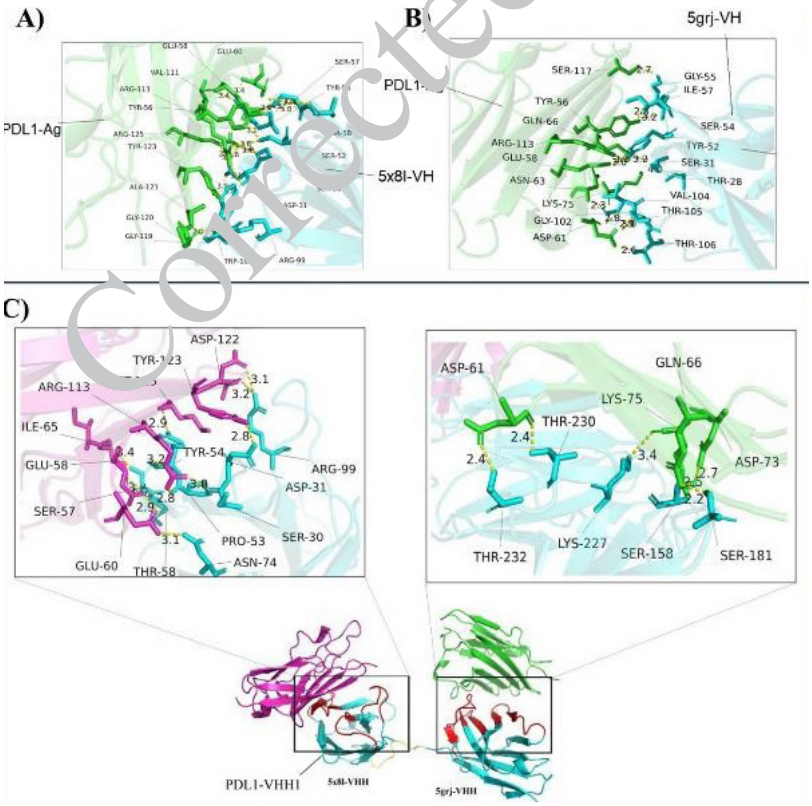


Figure 2. Comparative interaction analysis of PD L1 with different VH domains
(A) Detailed view of the binding interface between PD L1 antigen (PD L1 Ag; green) and the 5x8I VH domain (cyan). Interfacial residues are shown as sticks and labeled. Hydrogen bonds and close polar contacts are indicated by dashed yellow lines, with interaction distances given in Å. (B) Binding interface between PD L1 Ag (green) and the 5grj VH domain (cyan). Key interacting residues and hydrogen bond networks stabilizing the complex are highlighted and labeled, with distances shown in Å. (C) Binding interface of PDL VHH1 with the PD L1 antigen, with key interacting residues highlighted in the inset panels.

Corrected Proof

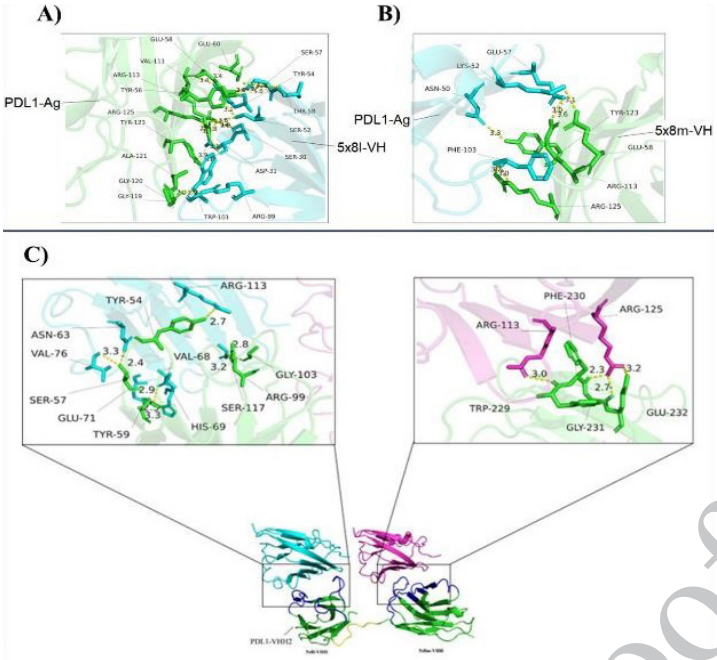


Figure 3. Structural comparison of PD L1 interactions with 5x8I VH and 5x8M VH domains
(A) Detailed view of the binding interface between PD L1 antigen (PD L1 Ag; green) and the 5x8I VH domain (cyan). Interfacial residues are shown as sticks and labeled. Hydrogen bonds and short range polar contacts are indicated by dashed yellow lines, with corresponding interaction distances given in Å. (B) Binding interface of PD L1 Ag (green) with the 5x8M VH domain (cyan). Key interacting residues involved in the molecular recognition of PD L1 are labeled, highlighting the changes in contact residues compared to the 5x8I VH complex. (C) Binding interface of PDL VHH2 with the PD L1 antigen. Insets depict the principal contact residues mediating nanobody–antigen recognition. Schematic overviews at the bottom of each panel indicate the regions enlarged in the insets.

positioned to bind to PDL1 at the same time, with the peptide linker offering adequate flexibility to facilitate dual binding. The structural visualization emphasizes the spatial configuration of CDRs and their accessibility to the PDL1 surface. As illustrated in Figure 2, structural modeling has identified distinct binding interfaces for PDL-VHH1 on PDL1. The detailed interaction maps reveal numerous hydrogen bond contacts, with critical residues establishing stabilizing interactions with PDL-VHH1. The recorded interatomic distances (2.6–3.9 Å) validate the close and stable interactions at the binding interface. In Figure 3, both PDL-VHH2 domains form multiple hydrogen bonds within 2.7–3.3 Å, indicating stable binding. The distinct sets of interacting residues identified in the docking models suggest that the two VHH domains may recognize adjacent or partially overlapping regions on the PD-L1 surface. However, these computational predictions require experimental validation to confirm epitope specificity and non-overlap.

Molecular dynamics (MD) simulation

To assess the structural stability and enhance the docking complexes, a 50 ns molecular dynamics (MD) simulation was conducted for the docked antiPDL1 VHHs, yielding insights into their conformational dynamics and interaction stability over time. The RMSD profiles (Figure 4A) indicated

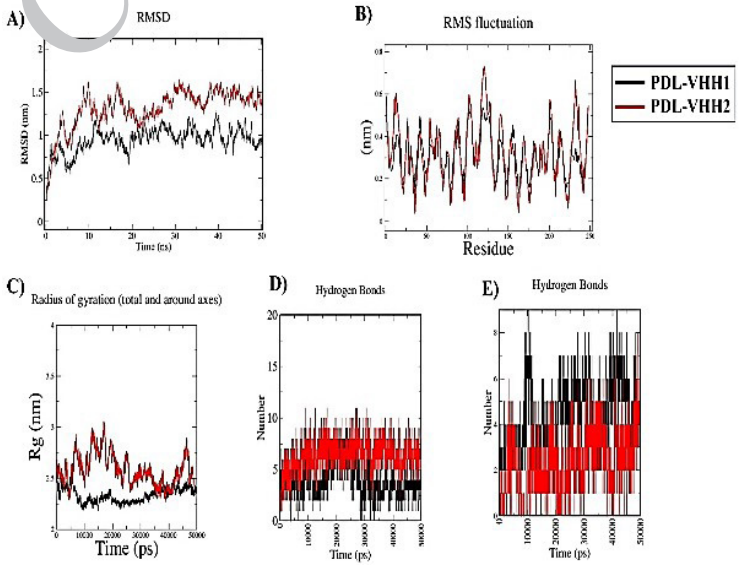


Figure 4. Molecular dynamics of the biparatopic nanobody constructs
A) Root mean square deviation (RMSD) calculations, B) Root mean square fluctuations (RMSF), C) Radius of gyration, D) Hydrogen bonds of 5x8l-VHH domains of biparatopic nanobodies with PD-L1 antigen, and E) Hydrogen bonds of 5grj-VHH and 5x8m-VHH domains of biparatopic nanobodies with PD-L1 antigen.

Corrected Proof

Table 1. Interface characteristics of biparatopic nanobody–PD-L1 complexes

Biparatopic nanobodies	Monovalent domain	Antigen	No. of interface residues [1]	Interface area (Å2)	No. of salt bridges	No. of hydrogen bonds	No. of non-bonded contacts
PDL-VHH1	5x8l-VHH	A	12: 13	583: 578	-	16	119
	5grj-VHH	A	14: 14	697: 608	2	10	167
PDL-VHH2	5x8l-VHH	A	12: 18	737: 705	-	6	107
	5x8m-VHH	A	12: 11	616: 556	1	4	124

Structural interface metrics for two biparatopic nanobody constructs (PDL-VHH1 and PDL-VHH2), each consisting of two monovalent segments targeting PD-L1. For each monovalent segment, the following parameters are reported: number of interface residues (presented as VHH residues: antigen residues), interface area (Å²), salt bridges, hydrogen bonds, and non-bonded contacts. PDL-VHH1 contains 5x8l-VHH and 5grj-VHH domains, whereas PDL-VHH2 consists of 5x8l-VHH and 5x8m-VHH. The data illustrate the distinct interaction profiles and binding contributions of each segment within the biparatopic configuration.
[1] No. of interface residues between VHH domain and antigen.

that PDL-VHH1 reached equilibrium sooner and remained stable with lower deviations, while PDL-VHH2 showed greater structural deviations over time, indicating lower conformational stability. Analysis of residue-level flexibility (Figure 4B) showed that PDL-VHH2 exhibited greater fluctuations across several loop regions than PDL-VHH1, although both constructs maintained relatively stable core regions. As shown in Figure 4C, PDL-VHH1 maintained a relatively stable, compact conformation throughout the 50 ns simulation, with Rg values fluctuating narrowly around a lower mean. Conversely, PDL-VHH2 showed higher Rg values and greater fluctuations, indicating reduced compactness and increased conformational flexibility. The number of intramolecular hydrogen bonds (Figures 4D and E) was consistently higher in PDL-VHH1 than in PDL-VHH2, with PDL-VHH1 showing more stable hydrogen-bonding patterns throughout the simulation. This implies stronger internal stabilization forces in PDL-VHH1.

Analysis of molecular interfaces in the biparatopic nanobody constructs revealed unique binding properties for each monovalent segment (Table 1). In PDL-VHH1, the 5x8l-VHH domain formed 12–13 interface residues, yielding an interface area of ~580 Å², supported by 16 hydrogen bonds and 119 non-bonded contacts, with no salt bridges. Conversely, the 5grjVHH domain interacted with 14 residues on both sides of the interface, exhibiting a larger buried surface area (~697/608 Å²) and stabilized by 2 salt bridges, 10 hydrogen bonds, and 167 non-bonded contacts. For PDL-VHH2, the 5x8lVHH domain showed broader interactions (12–18 residues) and the largest interface area (~737/705 Å²), but had fewer hydrogen bonds (6) and 107 non-bonded contacts, with no salt bridges. The 5x8mVHH domain formed contacts with 12–11 residues, yielding a moderate interface area (~616/556 Å²) stabilized by 1 salt bridge, 4 hydrogen bonds, and 124 non-bonded contacts.

MM/PBSA binding free energy calculations were performed to assess the thermodynamic stability of the nanobody–PD–L1 complexes quantitatively. As shown in Table 2, PDL-VHH1 exhibited a significantly more favorable binding free energy (–128.6 ± 3.5 kcal/mol) compared to PDL-VHH2 (–106.1 ± 4.1 kcal/mol), corresponding to a ΔΔG of –22.5 kcal/mol. The enhanced binding affinity of PDL-VHH1 is primarily attributed to its more favorable electrostatic interactions (–152.6 kcal/mol vs. –118.3 kcal/mol for PDL-VHH2), consistent with the greater number of hydrogen bonds and salt bridges identified at the PDL-VHH1 interface (Table 1). These computational predictions agree well with our experimental ELISA results, where PDL-VHH1 consistently showed stronger binding signals.

Table 2. MM/PBSA (Molecular Mechanics/Poisson-Boltzmann Surface Area) binding free energy components for PDL VHH1 and PDL VHH2 complexes with PD L1

Construct	ΔE_{vdW} (kcal/mol)	ΔE_{elec} (kcal/mol)	ΔG_{polar} (kcal/mol)	$\Delta G_{nonpolar}$ (kcal/mol)	ΔG_{bind} (kcal/mol)
PDL-VHH1	98.4±4.2	152.6±6.8	+135.2±5.1	12.8±0.9	128.6±3.5
PDL-VHH2	82.1±5.6	118.3±7.2	+104.5±6.3	10.2±0.8	106.1±4.1

ΔEvdW: van der Waals interaction energy; ΔEelec: electrostatic interaction energy; ΔGpolar: polar solvation free energy; ΔGnonpolar: non polar solvation free energy; ΔGbind: total binding free energy. Values are reported as mean±standard deviation. More negative ΔGbind values indicate stronger binding affinity

Production and purification of nanobodies

Recombinant VHH constructs were successfully cloned into the pET21b(+) vector and verified by colony PCR and sequencing. Following transformation into Origami (DE3) *E. coli* and induction of expression, SDSPAGE analysis revealed a prominent band at ~30 kDa, consistent with the predicted molecular weight of the VHH nanobodies. The solubilized pellets showed that the majority of the protein was localized in inclusion bodies. Crude lysates displayed the target protein along with bacterial contaminants, while NiNTA purification efficiently enriched the VHH constructs. Washing with 20 mM imidazole removed most nonspecific proteins, and final elution with 500 mM imidazole produced a strong, distinct ~30 kDa band with minimal background, confirming successful expression and purification of the recombinant nanobodies (Figure 5).

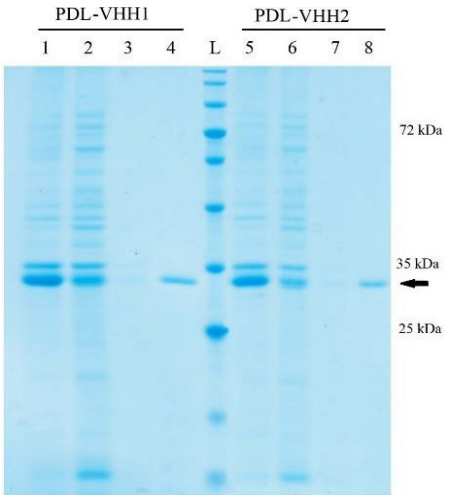


Figure 5. Expression and purification of nanobodies analyzed by 12% SDS PAGE
Lanes 1 and 5: whole cell lysates collected 8 h post induction; lanes 2 and 6: flow-through fractions after nickel affinity chromatography; lanes 3 and 7: eluates obtained with imidazole buffer; lanes 4 and 8: purified nanobody preparations. Lane L: molecular weight marker.

Corrected Proof

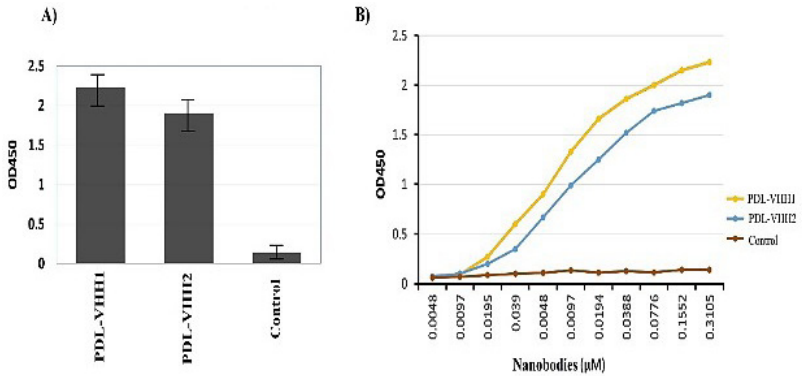


Figure 6. Binding activity of nanobodies PDL VHH1 and PDL VHH2 compared with control
(A) Indirect ELISA assay showing optical density at 450 nm (OD450) for PDL VHH1, PDL VHH2, and control samples. Both nanobodies showed significantly higher OD450 values than the control, indicating specific binding. (B) Dose response curves of nanobody binding, with OD450 plotted against nanobody concentration (0.0048–0.1505 μM). PDL VHH1 demonstrated the strongest binding signal across concentrations, followed by PDL VHH2, while the control remained at baseline levels.

Indirect ELISA

The binding activity of the refolded recombinant nanobody constructs against PD-L1 was assessed using indirect ELISA (Figure 6). All experiments were performed in triplicate, and specificity was rigorously confirmed using control wells lacking immobilized antigen. In the endpoint assay (Panel A), both PDL-VHH1 and PDL-VHH2 demonstrated specific and robust binding to immobilized PD-L1 when compared to the negative control wells, with PDL-VHH1 yielding the highest mean OD450 signal. In the concentration-dependent binding assay (Panel B), PDL-VHH1 showed a clear, dose-dependent increase in specific binding across the tested concentration range (0.0048–0.1305 μM) and achieved the highest absorbance values. PDL-VHH2 also showed clear, specific concentration-dependent binding to PD-L1, though with a lower maximal signal intensity relative to PDL-VHH1. The negligible absorbance observed in all no-antigen control wells confirmed the high specificity of the interaction for immobilized PD-L1.

Discussion

Generating nanobodies through traditional animal immunization or synthetic library screening is often resource-intensive and complex, creating a need for more streamlined design strategies (18). To address this, we employed a rational CDR grafting approach, transplanting the antigen-binding loops from clinically validated anti-PD-L1 antibodies (Atezolizumab, Avelumab, and Durvalumab) into the structural framework of the humanized nanobody, Caplacizumab. Our work aligns with the paradigm shift in nanobody engineering from simple monovalent nanobodies toward sophisticated multispecific constructs. As demonstrated by the successful engineering of humanized biparatopic anti-CD52 nanobodies (19), integrating computational modeling with CDR grafting can create agents with enhanced avidity and clinical potential. Furthermore, developing bispecific anti-PD-L1/VEGF nanobodies highlights the platform's unique ability to inhibit distinct yet synergistic disease pathways (20) simultaneously. These advancements, which demonstrate effective suppression of HUVEC and A431 cell growth by concurrently targeting PD-L1 and VEGF, confirm that nanobody modularity enables next-generation therapeutics that address the shortcomings of traditional monoclonal antibodies.

Structural analyses reveal distinct epitope targeting and specific molecular interactions between our VHH constructs and the canonical PD-L1 binding interface, providing a structural basis for their potential interaction with the PDL1 binding interface. Identifying distinct binding interfaces in our docking models is particularly significant, as it suggests the potential to engineer biparatopic molecules capable of synergistic binding. However, we acknowledge that these computational predictions must be validated experimentally to confirm that the two VHH domains indeed recognize non-overlapping epitopes on PD-L1. Future studies employing competitive ELISA or surface plasmon resonance (SPR) will be essential to confirm epitope specificity and to characterize the binding kinetics of our constructs (21). Shen *et al.* (2025) illustrate this principle, reporting that a biparatopic nanobody, CRNB909, showed significantly improved potency by simultaneously engaging two distinct epitopes. This resulted in the inhibition of TSLP binding to both TSLPR and IL-7Rα at the same time (22). Moreover, this multi-epitope targeting approach offers a strategic remedy for tumor immune evasion, a recognized clinical issue in which mutations at the PD-1/PD-L1 interface may confer resistance to monotherapy, as emphasized in structural research by Nowicki *et al.* (2018) (23).

The distinct structural dynamics of PDL-VHH1 and PDL-VHH2 highlight a key principle in biotherapeutics: the balance between rigidity and flexibility. PDL-VHH1 exhibited lower Rg, reduced RMSD, and more hydrogen bonds, indicating a more compact conformation. These features may influence stability and developability, though such properties cannot be directly inferred from simulations alone.

Conversely, the heightened conformational fluctuations observed in PDL-VHH2 are not intrinsically detrimental. This flexibility may support a consistent induced-fit model, potentially enabling the nanobody to adapt to conformational heterogeneity within the target epitope (24). Studies on other protein scaffolds support this phenomenon; for instance, Kong *et al.* demonstrated that regulated flexibility in antibody CDRs was essential for achieving high-affinity binding to a viral antigen (25). Consequently, while PDLVHH1 exhibited comparatively more compact structural behavior in the simulations, PDL-VHH2's intrinsic adaptability may offer distinct advantages for targeting specific, cryptic, or less-accessible epitopes on PD-L1 that require molecular plasticity for effective engagement. This contrast highlights the importance of MD simulations, which not only help select candidates but

Corrected Proof

also inform strategic decision-making (26). By clarifying dynamic profiles, we can rationally select a stable nanobody for effective blockade or a more flexible one for complex epitopes, guiding subsequent validation with biophysical techniques such as surface plasmon resonance to link nanobody dynamics to binding kinetics and therapeutic efficacy quantitatively.

Interface analysis revealed distinct binding mechanisms between the two constructs. PDL-VHH1 showed a well-balanced interaction profile: the 5x8l VHH domain contributed a dense hydrogen-bond network, while the 5grj VHH domain provided complementary stabilization through salt bridges and extensive non-bonded contacts. This combination of directional and electrostatic interactions may contribute to stabilization of the modeled interface, as the formation of salt bridges has been demonstrated to significantly improve binding affinity and thermal stability in engineered protein interfaces (27), a principle illustrated in the optimization of therapeutic antibodies by Xu *et al*. (28). In contrast, PDL-VHH2. However, it engages the largest interfacial area, primarily through its 5x8l VHH domain, and relies heavily on a broader range of non-bonded interactions, with relatively few hydrogen bonds and salt bridges. This interface, dominated by hydrophobic and van der Waals forces, often provides greater conformational flexibility, enabling the nanobody to accommodate target structural fluctuations, a characteristic observed in binders that interact with flexible loops (29). As a result, the enhanced directional stability attributed to the increased hydrogen-bond count in PDL-VHH1 provides a solid structural justification for its superior performance in our functional binding assays. These results establish PDL-VHH1 as the most appropriate candidate for therapeutic development in scenarios requiring a strong, stable blockade of PD-L1. At the same time, the flexible and adaptable interface of PDL-VHH2 should not be overlooked; its ability to interact with dynamic or cryptic epitopes could be utilized in biparatopic configurations, where its extensive interface may complement the precise, high-affinity anchor offered by PDL-VHH1, thereby forming a synergistic therapeutic approach with an increased resistance barrier. The successful development of anti-PD-L1 nanobodies, from expression to functional validation, illustrates an integrated pipeline that navigates common challenges in the development of biologic drugs.

Structural comparison of the parental monoclonal antibody VH domains and the corresponding CDRgrafted VHH constructs revealed a partially conserved binding mode toward PDL1. In particular, the overall orientation of the complexes and the dominant contribution of the CDR3 loop are maintained, with CDR3 engaging a similar functional surface region of PDL1 as observed in the parental VH–PDL1 complexes. However, despite the use of identical CDR sequences, clear differences in local binding geometry and interfacial contact networks are observed. These differences arise primarily from the distinct framework architecture of VHHs compared with conventional VH domains, most notably the absence of a paired VL domain and the intrinsic structural constraints of the VHH scaffold. As a consequence, CDR1 and CDR2 loops adopt slightly shifted conformations, with differences in loop flexibility and electrostatic surface distribution that reorient the antigenbinding site. This scaffolddependent reorganization enables the grafted VHH constructs to engage adjacent or partially overlapping surface regions of PDL1 rather than reproducing an identical epitope footprint. Importantly, these alternative interaction patterns still involve key PDL1 residues that contribute substantially to binding energetics, thereby supporting the preservation of antigen engagement despite differences at the residuelevel interface. Collectively, these results do not suggest that identical CDRs recognize unrelated epitopes; rather, they indicate a shifted or expanded interaction footprint within the same functional epitope region of PD-L1, consistent with previous reports showing that CDR grafting onto VHH scaffolds can preserve antigen recognition while modulating fine specificity through framework effects.

Recombinant VHH proteins often form inclusion bodies, necessitating denaturing purification, a common feature of high-yield microbial production systems. The literature extensively documents this phenomenon: rapid overexpression of disulfide-bonded proteins such as VHHs often overwhelms the bacterial folding machinery, leading to aggregation (30, 31). Our extraction of pure, though unfolded, protein through Ni-NTA chromatography under denaturing conditions provided the essential material foundation for subsequent functional characterization. The critical refolding process, accomplished by systematically removing denaturants in the presence of redox-shuffling agents, was crucial for restoring the antigen-binding paratope's native conformation and functional integrity, a well-established strategy for recovering proteins from inclusion bodies (32).

ELISA results indicate that the refolded nanobodies can recognize PDL1 under the tested conditions. PDLVHH1 produced stronger ELISA signals than PDLVHH2 across the tested concentrations, and this construct showed a more stable conformational profile and more stabilizing interfacial interactions in molecular dynamics simulations. While these observations are consistent with the structural trends observed in the simulations, ELISA measurements do not provide quantitative binding affinity or kinetic parameters (29, 30). This is particularly relevant in the context of recent advances in biparatopic nanobody design, exemplified by the work of Liu *et al*. on a biparatopic HER2-targeted nanobody, which demonstrated that biparatopic formats can not only block ligand binding but also actively modulate receptor clustering and internalization (33). Using these well-established design principles, our construct is a candidate for further investigation in studies evaluating checkpoint inhibition activity. The observed structural and functional synergy in our lead candidate, especially its compact conformational profile in simulations and stronger ELISA signal, offers a solid basis for further development as both a monotherapeutic agent and as a foundational element for more intricate multi-specific constructs. Future studies using surface plasmon resonance (SPR) will be needed to determine the precise dissociation constants (KD) and binding kinetics of PDL-VHH1 and PDL-VHH2, enabling a more rigorous comparison with clinically approved anti-PD-L1 antibodies.

Directly benchmarking each CDR-grafted VHH against its parental monoclonal antibody or corresponding scFv format would provide a quantitative measure of affinity and specificity retention after grafting. In this study, the focus was placed on structural feasibility and comparative binding modes of the grafted nanobodies using *in silico* modeling. Experimental comparison with parental or

Corrected Proof

clinically approved anti-PD-L1 antibodies was therefore not included. While our study successfully establishes a computational and experimental pipeline for the rational design of anti-PD-L1 nanobodies and confirms specific antigen binding via ELISA, functional validation of PD-1/PD-L1 checkpoint blockade is a critical next step. Future studies will employ cell-based assays, including Jurkat T-cell reporter systems and primary T-cell co-culture experiments, to quantitatively assess the ability of PDL-VHH1 and PDL-VHH2 to restore T-cell activation, proliferation, and effector cytokine secretion. Such functional data will be essential for advancing these candidates toward therapeutic applications.

Conclusion

This study successfully demonstrates the rational design and development of novel anti-PD-L1 nanobodies through an integrated approach of CDR grafting, molecular dynamics simulations, and experimental validation. We show that the engineered nanobody, PDL-VHH1, adopts a compact, stable conformation, forms numerous favorable interactions at the PD-L1 binding interface, and produces stronger ELISA signals than PDLVHH2 under the tested conditions. Despite the challenge of inclusion body formation, effective bacterial expression and purification yielded functional proteins suitable for characterization. Crucially, the ELISA results confirm the high specificity and dose-dependent binding of our constructs to PD-L1, supporting the feasibility of the computational design strategy. The structural characteristics observed for PDLVHH1 suggest it may be a candidate for further biophysical and functional characterization. Moreover, identifying a second, distinct binder in PDL-VHH2 provides a valuable component for constructing advanced biparatopic or bispecific formats. Collectively, our work not only delivers promising nanobody candidates for targeting the PD-1/PD-L1 immune checkpoint but also underscores the efficacy of structure-guided computational methods as a powerful pipeline for accelerating the development of next-generation biologics. Although the CDR grafting approach used in this study successfully transferred antigen-binding specificity to a stable VHH scaffold, this strategy has inherent limitations. Grafted CDRs may not adopt their native conformations in a different framework, potentially affecting binding affinity and specificity. Moreover, the absence of the VL domain in VHH scaffolds and their distinct framework architecture may impose structural constraints that computational modeling does not fully capture. Therefore, while our results confirm the feasibility of this approach for generating anti-PD-L1 nanobodies, experimental validation through SPR and cell-based assays will be essential to assess preserved binding characteristics and therapeutic potential fully.

Acknowledgment

The authors thank the Research Council of Yazd University, Iran, for supporting this research.

Data Availability Statement

Data sets used and/or analyzed during this study are available from the corresponding author upon reasonable request.

Funding

The Iran National Science Foundation (INSF) supported this study under project No. 4049627.

Ethical Approval

Not applicable.

Authors' Contributions

M M H designed the study, provided resources, conducted experiments, analyzed and validated the data, and drafted and revised the manuscript. E J N B and Z M conducted experiments and analyzed the data. M K conducted experiments, validated the data, and revised the manuscript. N A A and M Z conducted experiments and validated the data. All authors reviewed and approved the manuscript.

Conflicts of Interest

The authors declare that they have no conflicts of interest.

Declaration

The authors report that generative AI was not used in their research or preparation of this manuscript.

References

1. Sriharikrishnaa S, Suresh PS, Prasada KS. An introduction to fundamentals of cancer biology. Optical polarimetric modalities for biomedical research. 1st ed. Springer; 2023.
2. Wang X, Ding G, Tang Y, He J, Wang Q. Overcoming resistance to PD-1 and CTLA-4 blockade mechanisms and therapeutic strategies. Front Immunol 2025; 16:1-25.
3. Soltani M, Abbaszadeh M, Fouladseresht H, Sullman MJ, Eskandari N. PD-L1 importance in malignancies comprehensive insights into the role of PD-L1 in malignancies: from molecular mechanisms to therapeutic opportunities. Clin Exp Med 2025; 25:1-19.
4. Lin X, Kang K, Chen P, Zeng Z, Li G, Xiong W, *et al.* Regulatory mechanisms of PD-1/PD-L1 in cancers. Mol. Cancer 2024; 23:1-50.
5. Mitchell E, Pham MH, Clay A, Sanghvi R, Williams N, Pietsch S, *et al.* The long-term effects of chemotherapy on normal blood cells. Nat Genet 2025; 57:1684-1694.
6. Raja A, Kasana A, Verma V. Next-generation therapeutic antibodies for cancer treatment: advancements, applications, and challenges. Mol Biotechnol 2025; 67:3345-3365.
7. Almawash S. Revolutionary cancer therapy for personalization and improved efficacy: Strategies to overcome resistance to immune checkpoint inhibitor therapy. Cancers 2025; 17:1-63.
8. Pandey P, Khan F, Qari HA, Upadhyay TK, Alkhateeb AF, Oves M. Revolutionization in cancer therapeutics via targeting major immune checkpoints PD-1, PD-L1 and CTLA-4. Pharmaceuticals 2022; 15:1-17.
9. Davis AA, Patel VG. The role of PD-L1 expression as a predictive biomarker: An analysis of all US Food and Drug Administration (FDA) approvals of immune checkpoint inhibitors. J Immunother Cancer 2019; 7:1-8.
10. Saha D, Das PK, Veeranki VD. Developments in the production of recombinant monoclonal antibodies. Biotechnol J 2025; 20:e70127.
11. Evers A, Guarnera E, Pekar L, Zielonka S. From discovery to the clinic: Structural insights, engineering options, clinical, and 'next wave' applications of camelid-derived single-domain antibodies. mAbs; 2025; 17:e2583210.
12. Tang H, Gao Y, Han J. Application progress of the single domain antibody in medicine. Int J Mol Sci 2023; 24:1-18.
13. Saleem MZ, Jahangir GZ, Saleem A, Zulfiqar A, Khan KA, Ercisli S, *et al.* Production technologies for recombinant antibodies: Insights into eukaryotic, prokaryotic, and transgenic expression systems. Biochem Genet 2025; 63:3928-3967.
14. Heidari MM, Shirazi EA, Cheraghi SF, Shahshahani R,

Corrected Proof

Rahnama T, Khatami M. CDR grafting and site-directed mutagenesis approach for the generation and affinity maturation of Anti-CD20 nanobody. Mol Biol Rep 2024; 51:1-25.
15. Mirzaei M, Mirhoseini S, Heidari MM, Khatami M. Design and production of a novel anti-PD-1 nanobody by CDR grafting and site-directed mutagenesis approach. Mol Biotechnol 2025; 67:1843-1851.
16. Lizama-Muñoz A, Plaza-Diaz J. Bispecific antibodies, nanobodies and extracellular vesicles: Present and future to cancer target therapy. Biomolecules 2025; 15:1-23.
17. Wu W, Ali A, Sun L, Hu J, Hameed L, Shafi S, *et al.* Nanobodies: A promising toolkit for diagnostic applications. SmartMat 2026; 7:e70088.
18. Devasani JR, Guntuku G, sarabu P, Muthyala MKK, Palla MS, Subrahmanyam VM. Integrative and emerging models in antibody research: A comprehensive review. Antib Ther 2025:tbaf018.
19. Heidari MM, Khatami M, Soltanzade A, Rezaei S, Mirhashemi E. New strategy for the design and cloning of novel humanized biparatopic anti-CD52 nanobodies: Tools for targeted drug delivery and therapeutic approaches. Biochem Eng J 2025; 219:1-21.
20. Hassanzadeh Eskafi A, Oghalaei A, Mahboudi F, Ghaderi H, Behdani M, Shoari A, *et al.* Investigation of the therapeutic potential of recombinant bispecific bivalent anti-PD-L1/VEGF nanobody in inhibition of angiogenesis. Immunopharmacol Immunotoxicol 2023; 45:197-202.
21. Akiba H, Tsumoto K. Development and activities, including immunocomplex formation, of biparatopic antibodies and alternative scaffold proteins. Transl Regul Sci 2020; 2:1-6.
22. Shen H-L, Wang X-L, Liu Y-H, Chen C-J, Yin C-X, Yang Y-H, *et al.* Dual-epitope targeting of TSLP to simultaneously block TSLPR and IL-7Rα with a Biparatopic nanobody. Int Immunopharmacol 2025; 165:1-26.
23. Nowicki TS, Hu-Lieskovan S, Ribas A. Mechanisms of resistance to PD-1 and PD-L1 blockade. Cancer J 2018; 24:47-53.
24. Gupta A, Kao KS, Yamin R, Oren DA, Goldgur Y, Du J, *et al.* Mechanism of glycoform specificity and *in vivo* protection by an anti-afucosylated IgG nanobody. Nat Commun 2023; 14:1-11.
25. Kong L, Lee DE, Kadam RU, Liu T, Giang E, Nieusma T, *et al.* Structural flexibility at a major conserved antibody target on hepatitis C virus E2 antigen. Proc Natl Acad Sci 2016; 113:12768-12773.
26. Ou W, Dan J, Guo X, Liu Q, Tan L. An integrative strategy enhancing nanobody thermostability via CDR grafting, In silico mutagenesis screening, and multiplex evaluation. ACS Synth Biol 2025;14: 2690-2702.
27. Khan MF. Enhancing stability of enzymes for industrial applications: Molecular insights and emerging approaches. World J Microbiol Biotechnol 2025; 41:1-28.
28. Xu AY, Blanco MA, Castellanos MM, Meuse CW, Mattison K, Karageorgos I, *et al.* Role of domain–domain interactions on the self-association and physical stability of monoclonal antibodies: effect of pH and salt. J Phys Chem B 2023; 127:8344-8357.
29. El Salamouni NS, Cater JH, Spenkelink LM, Yu H. Nanobody engineering: Computational modeling and design for biomedical and therapeutic applications. FEBS Open Bio 2025; 15:236-253.
30. Ban B, Sharma M, Shetty J. Optimization of methods for the production and refolding of biologically active disulfide bond-rich antibody fragments in microbial hosts. Antibodies 2020; 9:1-18.
31. Nakic M. Optimization of *Escherichia coli* expression, purification and characterization of antibody fragments [dissertation]. Zagreb: University of Zagreb, Faculty of Food Technology and Biotechnology; 2023.
32. Phelps [illegible] Hetherberg LK. Protein disaggregation and refolding using high hydrostatic pressure. J Chem Technol Biotechnol 2007; 82:61[illegible]613.
33. Liu [illegible] Guo L, Wang Y, Meng X, Shao Y, Fan X, *et al.* Biparatopic HER[illegible]-targeted nanobody binder synergizes with trastuzumab in resistant tumor cells. Front Immunol 2025; 16:1-15.

Corrected Proof